First post-mortem analysis of deposits collected on ITER-like components in WEST after the C3 and C4 campaigns

Céline Martin, Mathilde Diez, Andrea Campos, Martiane Cabié, Gregory Giacometti, Martin Balden, Alberto Gallo, Bernard Pegourié, Elodie Bernard, Emmanuelle Tsitrone

First post-mortem analysis of deposits collected on ITER-like components in WEST after the C3 and C4 campaigns

Celine Martin[1], Mathilde Diez[2], Andrea Campos[3], Martiane Cabié[3], Gregory Giacometti[1], Martin Balden[4], Alberto Gallo[2], Bernard Pegourié[2], Elodie Bernard[2], Emmanuelle Tsitrone[2] and the WEST team[*]

[1] Aix-Marseille University, CNRS, PIIM UMR 7345, Marseille, France
[2] CEA, IRFM, F-13108, Saint-Paul-Lez-Durance, France
[3] Aix-Marseille University, CNRS, Centrale Marseille, FSCM, CP2M, Marseille, France
[4] Max-Planck-Institut für Plasmaphysik, Boltzmannstr. 2, 85748 Garching, Germany
[*] See http://west.cea.fr/WESTteam

E-mail: celine.martin@univ-amu.fr

Abstract

In order to map the complex plasma footprint observed on the lower divertor of the WEST experiment after its first phase of operation, we analysed deposits collected on ITER-like Plasma Facing Units (PFUs) exposed in the C3 (deuterium plasma) and C4 (deuterium and helium plasma) campaigns. Our results show that these deposits have multilayer structures mainly composed of tungsten, oxygen, boron and carbon, whose texture and composition vary along the radial direction. These traits allowed us to identify three types of deposits: deposits rich in boron (conditioning) in the low plasma flux area further away from the strike point, deposits rich in tungsten with traces of metallic compounds (Cu, Fe, Cr, Ni, Ag) in the high plasma flux area and deposits rich in boron and tungsten in the private flux area. In addition, we found more nanoparticles, voids and tungsten oxide layers in the deposits formed during C4 in comparison to that of C3.

Keywords: WEST, deposits, divertor, erosion, redeposition

1. Introduction

After five experimental campaigns (referred as C1 to C5), the first phase of operation of WEST (2017-2020) has come to an end [1,2]. A vast post-mortem analysis program is now starting on the plasma-facing components to better understand plasma-surface interactions in a full-tungsten (W) environment. These characterization studies focus more particularly on the components of the lower divertor for which careful monitoring is ensured by a wide set of in-situ diagnostics [3,4,5].

During this first phase of operation, the lower divertor of WEST consisted of inertial W-coated graphite tiles and water-cooled ITER-like plasma facing units (PFUs) made of 35 bulk W monoblocks (MBs) bonded to a CuCrZr tube that were progressively installed into the vacuum vessel. A visual inspection of the lower divertor after the C3 and C4 campaigns revealed a complex plasma footprint with clean monoblock surface around the inner strike point (ISP, MB14-18) and outer strike point (OSP, MB24-28) areas while a deposition-dominated area was observed on the inner side of the divertor (MB 1-13) [6] as predicted by modeling [7]. This paper aims at investigating the modification of the PFUs surface properties in order to better characterize erosion/deposition patterns on the divertor. To this end, deposited layers were collected from monoblocks distributed along the radial (WEST major radius) and toroidal directions in the deposition-dominated area of the divertor and their properties (composition, thickness, morphology, adhesion) were analyzed to better understand material migration in WEST. The effect of the helium plasma exposure (performed during C4) and boronization on the deposition process is also investigated.

2. WEST configuration

Figure 1 shows a view of the inner vessel of WEST, with the lower divertor where the ITER like PFU are installed (configuration for the C3 campaign shown here). The ITER like PFU MB numbering is indicated, with MB1 located on the High Field Side (HFS) and MB35 on the Low Field Side (LFS). A typical magnetic equilibrium of WEST is also presented, showing the inner and outer strike points (ISP and OSP respectively) located on the same target. The typical strike point position in WEST is between MB14 and MB18 for the ISP and MB24 to MB28 for the OSP.

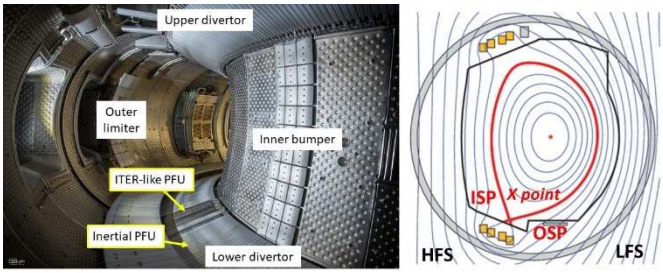

Figure 1: Photograph of the WEST vessel during phase 1 operation (before the start of the C3 campaign in 2018), showing the lower divertor equipped with a mix of ITER like actively cooled bulk W PFU and inertial W coated PFU. Typical magnetic equilibrium in WEST, showing the inner and the outer strike points located on the same target is depicted in the right hand side of the figure.

WEST was progressively equiped with ITER like PFU, located on one of the 12 modular lower divertor sectors (test divertor sector Q3B). Figure 2 shows the configuration of the test divertor sector Q3B for the C3 and C4 campaigns, and the location of the PFU where deposits have been collected.

The plasma load pattern on the divertor of WEST is modulated by the magnetic field ripple, with alternating maximum load areas on the HFS and LFS (see for instance [8] for the description of the ripple impact on the plasma loads in WEST). On the test divertor sector where the ITER like PFU are implemented, the most loaded area on the LFS is around PFU7 and PFU32 toroidally, in the OSP position radially (so called max OSP area), while the most loaded area on the HFS is around PFU20 toroidally, in the ISP position radially (so called max ISP area). This is illustrated in Figure 2.

In terms of plasma exposure, the C3 campaign was the first campaign with significant cumulated plasma duration (~2h of deuterium (D) plasma exposure, to be compared with less than ~30 minutes for C1 and C2) and power coupled to the plasma (up to ~5 MW of Lower Hybrid (LH) power for C3, to be compared with 2.5 MW for C1-C2). First boronizations were performed in C3 (3 boronizations). In the C4 campaign, the coupled power was raised up to 9 MW of combined LH and ICRH power, and both D and helium (He) operation were performed, with more than 2.5 hours of D exposure and ~45 minutes of He exposure. In particular, a dedicated He phase was performed at the end of the C4 campaign to investigate He-W plasma-wall interactions, using repetitive shots (~30 minutes of He operation) to load the lower divertor with He [2], in contrast with other WEST operation phases, where the plasma scenarios are varied. During this phase, the ISP was located on MB14 from the magnetic reconstruction, but the maximum He fluence was recorded around MB10 from Langmuir probe data analysis [2]. Boronizations were perfomed regularly during C4 (13 boronizations), but not during the last phase of He operation.

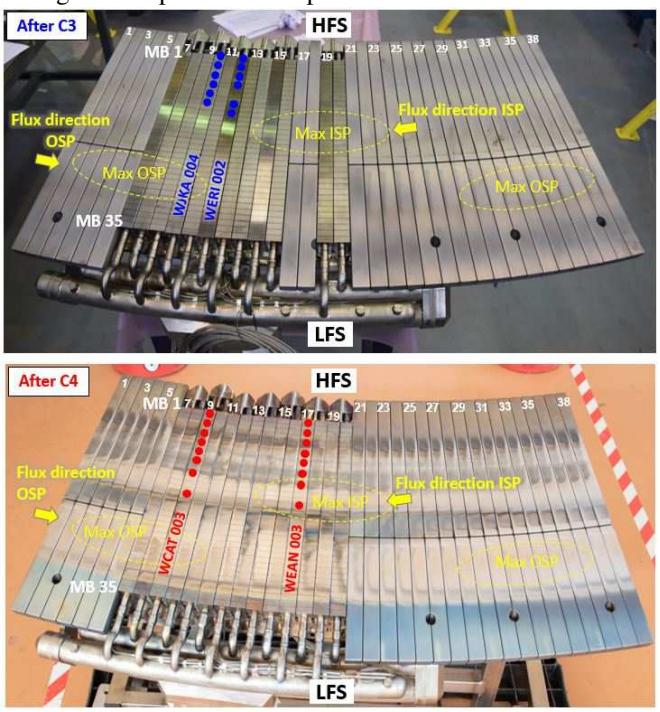

Figure 2: Configuration of the WEST test divertor sector for the C3 campaign with 12 ITER like PFU (top) and for the C4 campaign with 14 ITER like PFU (bottom). The PFU numbering on the sector (from 1 to 38) is indicated as well as the PFUs where the deposits have been collected after the C3 and C4 campaigns. Finally the areas of maximum plasma loads alternating on the HFS (max ISP) and LFS (max OSP) due to the impact of the magnetic ripple are shown.

3. Experimental procedure

3.1 Collection procedure

The deposits were retrieved on 2 PFUs, namely WJKA004 (located at position PFU10) and WERI002 (located at position PFU12), at the end of the C3 campaign (WERI002 was exposed during C3 only while WJKA004 was exposed during C1, C2 and C3). It should be noted that WERI002 was significantly misaligned during the C3 campaign (up to 0.8 mm in the OSP area), while WJKA004 was aligned within specifications (see [9] for a description of PFU misalignement during C3). In addition, deposits were collected at the end of the C4 campaign on PFU WEAN003, located at PFU17. WEAN003 was exposed during C4 only, and was misaligned within ITER specifications (0.3 mm in the OSP area). Deposits on one additional PFU were collected after C4 (WCAT003, located at PFU09), but results are not discussed here, as it was exposed to both C3 and C4. Due to maintenance

operations, the lower divertor sector Q3B was taken out of the vacuum chamber and the collection was performed ex-situ, 3 months after the end of C3 and 6 months after the end of C4. On the same PFU, deposits were collected at different radial positions (MBs 1,3,5,7,9,11,13) in the deposition dominated area using a tape sampling method consisting in pressing manually (5-10 sec) a SEM sample holder covered with a double-sided adhesive carbon tape onto the monoblock surface area. For WEAN003, deposit was also collected on MB 17 because visual inspection seemed to suggest deposition in this area after C4 despite the fact that MB17 is located in the ISP area. Indeed, specific plasma experiments carried out during C4, including the He campaign, have resulted in the move of the strike point in the radial direction, leaving MB17 sometimes exposed to the plasma, sometimes in the private flux region. The table presented in figure 3 gives the details of the collection samples.

Figure 3 shows PFU WEAN003 after the deposits were collected and transferred to carbon tape for direct analysis, and the table given below Figure 3 details the MB collected on each PFU. With this collection method, the top layer on the sample holder (refered as 'first layer' in the following of the paper) corresponds to the layer formed earliest in the history of the campaign. The underneath layers correspond to the layers formed later on during the exposure. It should be noted that this 'first layer' truly corresponds to the first layer formed onto the PFU surface during the campgnain only when the entire stack of deposit is removed.

This collection method does not require additional sample handling or material cutting that could pollute the deposits and could therefore be used in-situ. In addition, the amount of deposit detached from the surface gives qualitative information about the adhesion level of the deposits to the PFU. Using confocal microscopy, the surface area of the SEM sample holder was analysed after the collection procedure. The level of adhesion of the deposits was qualified as 'low' when the deposits covered more than 60% of the sample holder surface area. It was qualified as 'strong' when the deposits covered less than 10% of the holder surface area. In between, the level of adhesion was qualified as 'medium". As a first approximation, the level of adhesion of deposits can be related to their ability to become mobile in the vacuum chamber.

In the future, a method should be deployed (i) to better control the sample holder pressure applied onto the PFU (ii) to measure precisely the force required to detach the sample holder from the PFU and (iii) to check the complete removal of deposit.

3.2 Characterization tools

The deposits were analyzed using scanning electron miscroscopy (SEM, Zeiss Gemini SEM500) coupled with Energy Dispersive X-ray (EDAX SDD detector). Backscattered electron (BSE) images or secondary electron (SE) images were collected to highlight the chemical or topograghic contrast. Spectra were collected during 200 s at 5 kV incident energy for the detection of B, W, C and O and at 15 kV for the detection of metal traces.

Two of the samples (MB 11 WJKA004 and MB 11 WEAN003 collected respectively after C3 and C4) were also cut by focused ion beam (FEI Helios 600 NanoLab) so that the deposited layer cross section could be examined by scanning transmission electron microscopy (STEM, FEI Tecnai G2) coupled with EDX (Oxford XMax80).

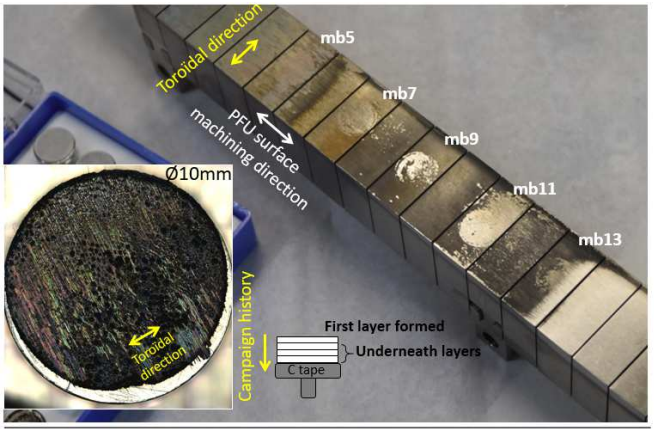

	MB1	MB3	MB5	MB7	MB9	MB11	MB13	MB17
WJKA004 *Exposed to C1-C2-C3*	o	o	o	o	o	o		
WERI002 *Exposed to C3 only*	o	o	o	o		o	o	
WEAN003 *Exposed to C4 only*	o	o	o	o	o	o	o	o
WCAT003 *Exposed to C1-C2-C3-C4* (not discussed in this paper)	o	o	o	o	o	o	o	o

Figure 3: Photograph of PFU WEAN003 taken after the deposits have been collected using the SEM holder. Inset showing a photograph of the SEM sample holder with the deposit on the carbon tape. The table below details the MB's where deposits have been collected for each PFU.

4. Results

4.1 Analysis of deposits by SEM-EDX

4.1.1 Morphology. All the deposits exhibit a multi-layer deposition structure, with layers of different morphology. Figure 4 shows SEM images of the deposits collected after the C3 campaign on PFU WJKA004 (Fig. 4b, Fig. 4c and Fig. 4d) and WERI002 (Fig. 4a). The direction corresponding to the toroidal direction in the WEST vacuum vessel is indicated on the micrographs. The first layer deposited at the beginning of the campaign is also indicated by ①. The images of deposits collected on MB 5 (a), MB 11 (b) were taken with the same magnification so that the morphology of the deposits can easily be compared along the radial direction. From MB 1 to MB 7 deposits are generally rough and a homogeneous structure can be observed (see Fig.4a). The first layer is cracking. The deposits had a 'strong' (or 'medium' for MB 7)

adhesion to the PFU surface resulting in a low amount of deposit collected which leaves the C tape visible (see the dark contrast on Fig.4a). From MB 9 to MB 13, a homogeneous structure is observed. The first layer is smooth with few cracks and is peeling off (Fig.4b). The deposits were easily detached from the PFU surface during the collection procedure (low adhesion).

Fig.4(c) and (d) show images taken at high magnification of multilayers and nanostructures observed on the deposits after C3. Fig.4c shows a deposit with thin layers of different textures alternatively smooth or with nano-particles inducing a rough texture. Fig.4d shows a cross section of a deposit scrap with also thin layers of different textures which are delaminated.

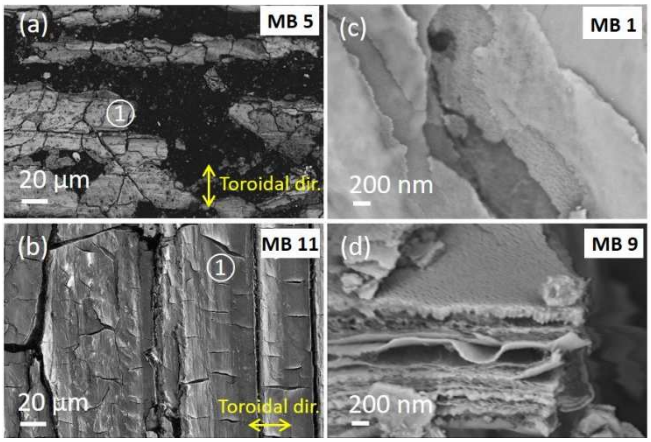

Figure 4: SEM images (BSE mode) showing the morphology of the deposits collected after the C3 campaign on (a) WERI002 MB 5 (b) WJKA004 MB 11 (SE mode for this image only). On the right hand side, high magnification images of WJKA004 (c) different textures found in the first layers of MB 1, (d) thin layers of different texture found in a deposit scrap observed by its section.

Figure 5 shows SEM images (BSE mode) of the deposits formed during the C4 campaign on PFU WEAN003. The images of deposits collected on MB 5 (a), MB 11 (b) and MB 17 (c) were taken with the same magnification so that the morphology of the deposits can easily be compared along the radial direction. From MB 1 to MB 5 deposits are generally smooth and a homogeneous structure can be observed (see Fig.5a). The first layer is peeling off. The deposits had a 'medium' adhesion to the PFU surface. From MB 7 to MB 11, a non-homogeneous structure is observed. The first layer is quite smooth with localised W-rich areas (see the bright contrast on Fig.5b). The deposits were easily detached from the PFU surface during the collection procedure (low adhesion). On MB17 deposits are found to have an anisotropic morphology since alternative bright W-rich and dark B-rich layers formed along the PFU machining groove direction. The deposits have a low adhesion to the PFU surface.

Fig. 5(d) to (f) show images taken at high magnification of nanostructures observed on the deposits after C4. Fig.5d shows layers of nanoparticles with sizes about 10-20 nm found into the first layer of MB 1. Fig.5e shows larger metallic particles with sizes about few tens of nm found into the underneath layer of MB9. Fig.5f shows nano-holes at the deposit surface of MB17 with sizes about 20-50 nm which may suggest a formation of nanobubbles under helium implantation as previously observed on W surfaces or at WO_3/W interface [10-13]. Nevertheless, even if this observation could be expected following a Helium plasma exposure, similar observations during the Helium-free campaign also gave rise to the evidence of porosities [14]. Therefore, a more extensive post-mortem study is needed to determine the origin, location and size of the different porosities observed after the He campaign. Indeed, bubbles could also be created by other elements co-deposited or outgassed from the PFU surfaces which would diffuse into the deposits and which due to their low solubility could also give rise to the formation of holes and porosity.

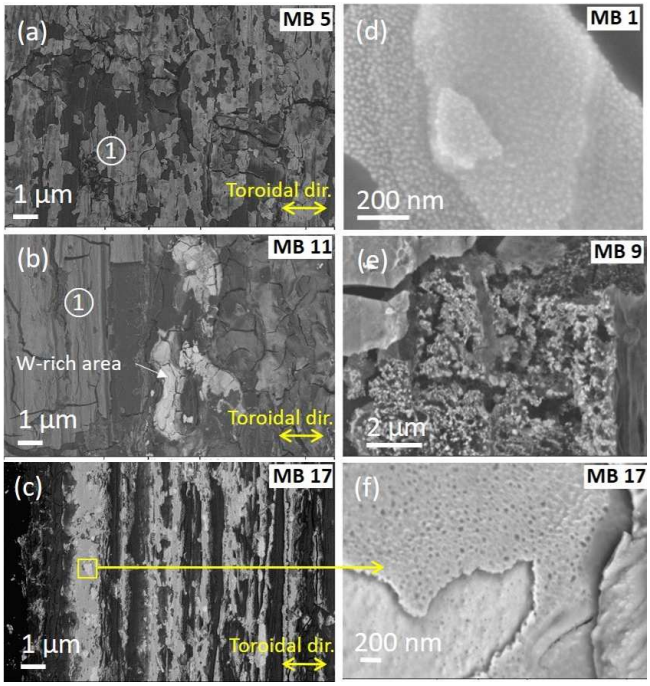

Figure 5: SEM images (BSE mode) showing the morphology of the deposits collected after the C4 campaign on WEAN003 (a) MB 5 (b) MB 11 and (c) MB 17. On the right hand side, high magnification images of (d) nanoparticles found in the first layer of MB 1, (e) particles in the underneath layer of MB 9 (f) nano-holes in a W-rich layer of MB 17.

4.1.2 Chemical composition. A comparative chemical analysis was performed by EDX on the first layer and the underneath layer of all the collected deposits as the SEM-EDX quantification is not accurate without depth absorption modeling on surfaces and stacked thin films. Figure 6 and 7 show the results obtained on MB 7 and MB 11 of WJKA004 (C1 to C3 exposed) and of WEAN003 (C4 exposed), respectively.

All the deposits contain W and O, whilst B and C were detected with varying contents depending on their radial position. W originates from W migration during the campaign.

Oxygen may have the same origin since it is detected in-situ but post-campaign oxidation must also be considered.

Deposits collected after C3 can be classified into 2 categories. From MB 1 to MB 7, the first layer is composed of W and O while the underneath layer contain B and C (see Fig.6a). From MB 9 to MB 11 the first layer is also composed of W and O but the underneath layer is rich in W. Almost no B and C are detected (see Fig.6b).

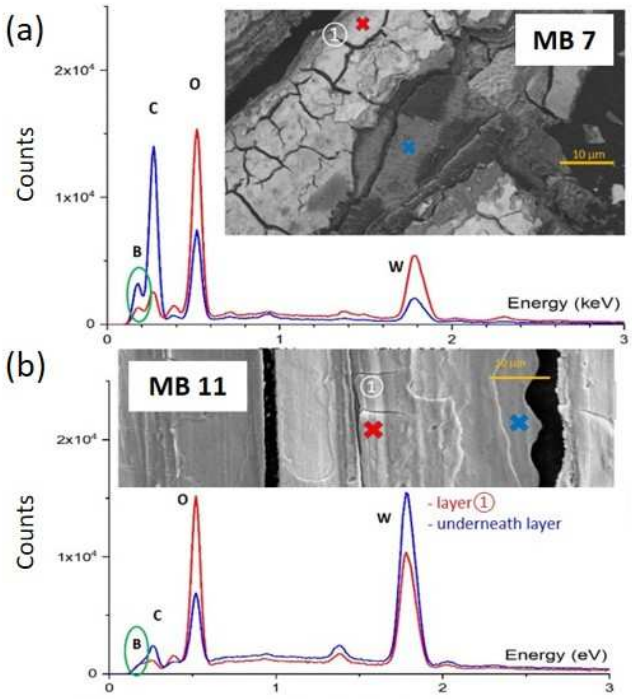

Figure 6: EDX spectra of the first layer (red) and the underneath layer (blue) for deposits collected after C3 on WJKA004 (a) MB 7 (b) MB 11.

Deposits collected after C4 (see Fig.7a and 7b) contain generally more B than that collected after C3 (see Fig.6a and 6b). This can be explained by the large number of glow discharge boronizations performed during the C4 campaign (13 boronization in C4 vs 3 in C3). It is also interesting to see that the deposits collected at the same radial position (MB 11) exhibit different chemical compositions depending on the plasma operation. The first layer that formed during C1-C3 is a tungsten oxide layer and the underneath layer is rich in W (see Fig.6b), while the first layer that formed during C4 is a tungsten oxide layer and the underneath layer is rich in B and C (see Fig.7b). The tungsten oxide layers were even more clearly identified thanks to STEM measurements coupled to EDX on FIB lamellas which allows quantification (see section 3.2). It appears that the carbon content correlates with the boron content, which shows that the deposits collected after C4 contain more carbon than those collected after C3 in agrement with the results of deposits analysed on the inner W-coated PFU [14]. One of the main sources of C in WEST is the exposure of graphite substrate of the inertial tiles on the lower divertor as the result of the W coating delamination [6]. However, most of the delamination occurred during C3 which could indicate that the erosion of the graphite substrate is the source of this C. Another source of C could also be the boronization procedures but at this stage these are only assumption and this effect is not yet understood.

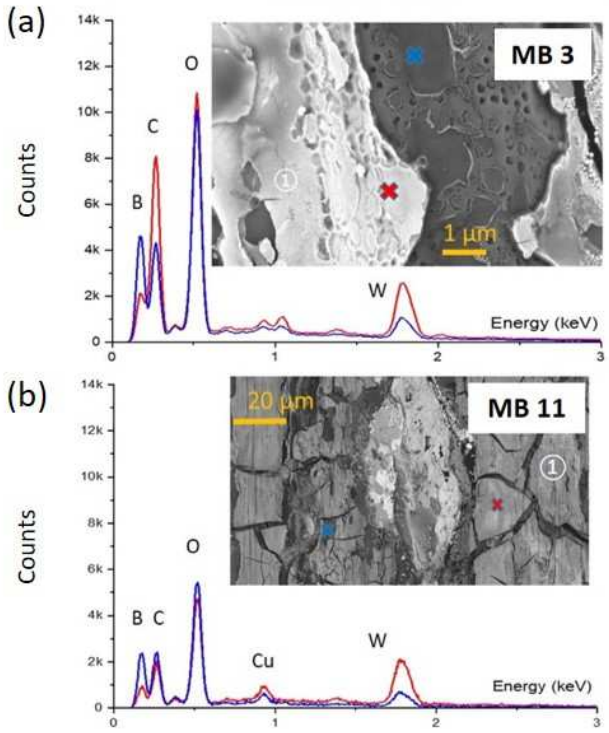

Figure 7: EDX spectra of the first layer (red) and the underneath layer (blue) for deposits collected after C4 on WEAN003 (a) MB 7 (b) MB 11.

	After C3 campaign				After C4 campaign			
		Adhesion	Morphology	Composition		Adhesion	Morphology	Composition
Low flux	MB 1-7	strong medium	homogeneous rough and cracking Fig.4a and Fig.6a	B and C-rich layers Fig.6a	MB 1-5	strong medium	homogeneous smooth and peeling off Fig.5a and Fig.7a	B and C-rich layers Fig.7a
High flux	MB 9-13	low	homogeneous smooth and peeling off Fig.4b and Fig.6b	W-rich layers no B and C Fig.6b	MB 7-13	low	non homogeneous smooth and cracking Fig;5b	W-rich area B and C-rich layers Fig.7b
ISP/Private					MB 17	medium	Anisotropic Fig.5c	W-rich B and C-rich

Table 1: Adhesion, morphology and chemical composition of the deposits identified in the three locations of the lower divertor.

Finally, it was found that all deposits collected on MB 3 to MB 11 contain elements from the antennas (Cu) and the stainless steel wall (Fe, Cr, Ni), for both C3 and C4 exposed PFU. Traces of Al, P, S, Ag and Cl were observed in small quantities in that same area.

In order to study the evolution of W and B content along the PFU, the maximum peak intensity of these elements obtained in the first layer of WEAN003 was measured and plotted as a function of the monoblock number (figure 8). It can be seen that the boron content is high in MB 1 and decreases when approaching the strike point region. Whereas the W content increases close to the strike point area with the highest peak intensity measured for MB 13. Note that the oxygen profile (not shown here) is similar to that of the boron, indicating the correlation between the oxygen content and boronisations.

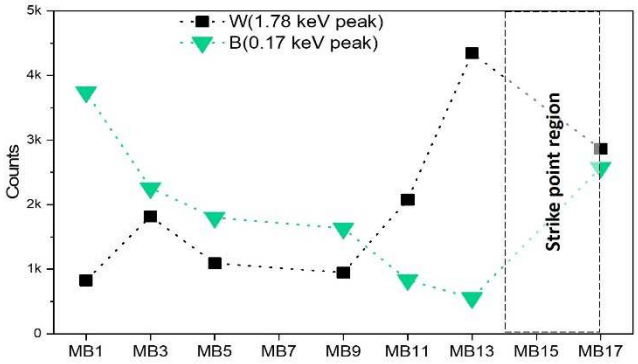

Figure 8: Evolution of EDX spectra peak intensity of W and B as a function of the MB number measured on PFU WEAN003 after the C4 campaign.

4.1.3 Summary of SEM-EDX analysis. The SEM-EDX results allowed us to identify 3 types of deposits associated with different areas on the inner side of the lower divertor, referred as low flux area, high flux area and private flux region. Table 1 reports the properties of the deposits in these areas in terms of adhesion, morphology and chemical composition. Based on our observations the high flux area, where the deposits are thick and have a low adhesion to the monoblock surface, seems to have expanded between C3 and C4 (MB 9-13 vs MB 7-13). The post-mortem analysis conducted on the erosion marker tiles of the lower divertor of WEST led to the same result [14]. The extension of this deposition zone during C4 can be explained by the change of the magnetic equilibrium configuration.

4.2 Analysis of deposits as a function of depth

The SEM analysis has evidenced a multi-layer structure of the deposits even though the first layers only were able to be analyzed. In order to evaluate the thickness of the deposits, the number of layers and to quantify the oxides thinned-FIB lamellas were extracted on MB11 on WJKA004 and WEAN003 and analyzed by TEM.

Figure 9a and 10a show the STEM images of the cross-section of the deposits formed during the C1-C3 campaigns and the C4 campaign, respectively. The different layers can be identified by the grey and black contrast. It can be seen that the deposits formed during C1-C3 consist in well-defined and smooth layers. However, voids exist between the layers. It corresponds to delamination of the grey layers, for which the morphology and composition may represent a weak point. After C4, more voids can be seen in the deposits. The layers seem to be in the process of tearing off. Based on these images, the total deposits thickness (without including voids) can be estimated at about 1 µm after C1-C3 and 3±0.5 µm after C4, respectively. The large presence of voids in the deposits collected after C4 brings some uncertainties in the thickness measurement.

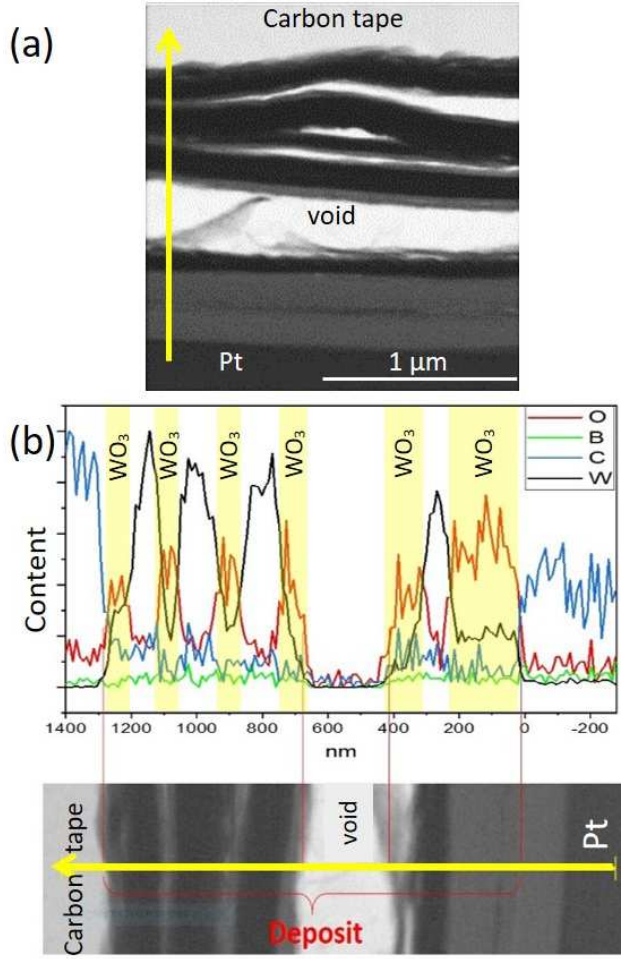

Figure 9: STEM bright field image (a) and (b) EDX depth profiling of FIB-thinned lamella extracted from MB 11 on WJKA004 after C3.

A depth profile analysis was then performed using EDX at the location corresponding to the yellow line indicated on the STEM images. Figure 9b shows the line profiling after C3. A total of 10 layers can be identified, with an alternation of 4 W layers (of about 100 nm thick) and 6 oxidized W layers (WO_3 type). In the middle of one oxidized W layer delamination occurs showing a large void.

The depth profile obtained for the deposits formed during C4 is depicted in figure 10b. At least 5 tungsten oxide layers can be identified, with thickness ranging from 100 nm to 500 nm. Unlike the C1-C3 deposits, no pure tungsten layer is detected whereas C-rich layers are present. In addition, it can be seen that traces of B are present in the first 1-1.5 µm and tend to disappear in the last third of the deposits (signal reduced to noise level). This corresponds well to the C4 campaign history during which boronisation was used during the two thirds of the campaign then stopped during the helium phase at the end of the campaign. The presence of carbon in some areas near the voids may originate from the carbon tape during the lamella preparation.

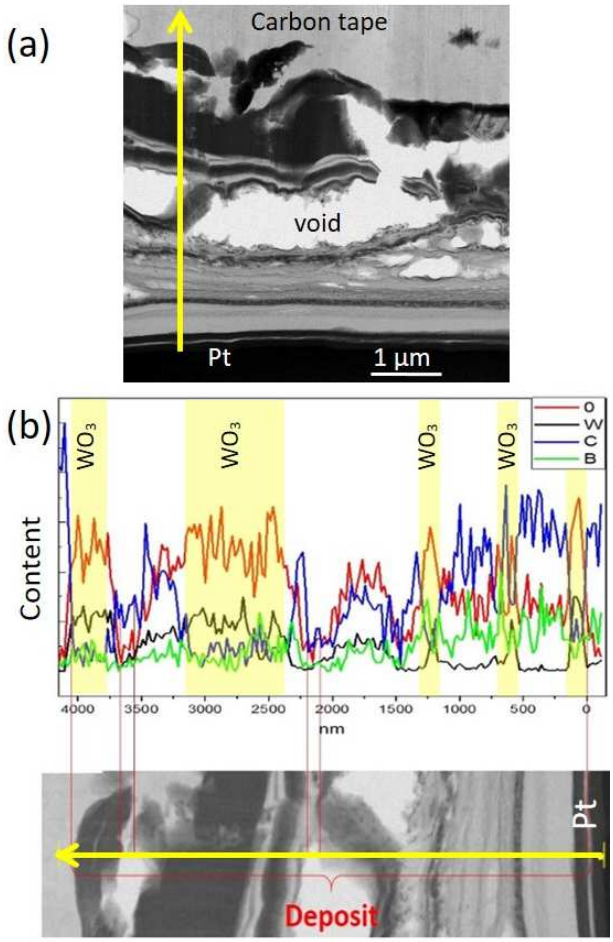

Figure 10: STEM bright field image (a) and (b) EDX depth profiling of FIB-thinned lamella extracted from MB 11 on WEAN003 after C4.

5. Conclusion

In this paper we used a promising technique for in-situ collection of deposits that formed during the operating of WEST. The characterization of these deposits allowed identifying two types of deposition areas on the inner side of the lower divertor although the erosion/redeposition pattern in WEST turned to be out more complex than previously studied in Tore Supra [15]. These deposition areas do not always reflect the contrast areas observed on the PFUs during the visual inspections of the divertor [14].

In the low flux area (MB 1-7 for C3 ; MB1-5 for C4), the first layer of deposits that formed during operation is rich in boron, which reflects the use of boronisation during each campaign. However, there is a radial distribution of the amount of boron and tungsten in the first layer. Boron content is high in the MB1-3 area but tend to disappear when approaching the strike line region. In parallel an increase of tungsten content occurs when approaching the strike line region. This would suggest the erosion of the boronized layer by the plasma and the redeposition of tungsten.

In the high flux region (MB 9-13 for C3 ; MB 7-13 for C4), a multi-layer structure was clearly evidenced, with the large presence of tungsten oxide layers. The deposits formed during C1 to C3 are about 1 µm thick and consist mainly of an alternation of tungsten and tungsten oxide layers. The deposits formed during C4 are 3±0.5 µm thick and are composed of tungsten oxide layers with boron detected only in the first layers. Metallic nanoparticles were also found in most of the deposit layers.

It is therefore clear that the main elements found in the deposits not only originate from the materials used for the PFCs (W, C) but also come from the conditioning of the vacuum chamber (B, O), resulting in the formation of tungsten oxide layers. The amount of oxygen in the deposits was also found to be correlated with the number of boronizations, as its presence was much higher after C4 than after C3 (3 boronizations during C3 vs 13 boronizations during C4).

These results will now be correlated with the plasma conditions in WEST coupled with modeling in order to explain the differences in the deposits morphology after C3 and C4 and better understand the role of boron and helium in plasma-wall interaction. Indeed, post-mortem analysis characterizing the erosion/deposition pattern coupled with the understanding of synergistic effects of particle and heat loading of ITER-grade W [16] is a key topic for future reactors like ITER that will operate with actively cooled bulk tungsten monoblocks.

Acknowledgements

This work has been carried out within the framework of the EUROfusion Consortium and has received funding from the Euratom research and training programme 2014–2018 and 2019–2020 under grant agreement No. 633053. This work was performed under EUROfusion WP PFC.

References

[1] BUCALOSSI J. et al., Operating a full tungsten actively cooled tokamak: overview of WEST first phase of operation, presented at IAEA 2021

[2] TSITRONE E. et al., Investigation of plasma wall interactions between tungsten plasma facing components and helium plasmas in the WEST conference, presented at IAEA 2021
[3] GASPAR J. et al., Nuclear Materials and Energy 25 (2020) 100851
[4] FEDORCZAK N. et al., Nuclear Materials and Energy 27 (2021) 100961
[5] HOURY M. et al., Fusion Engineering and Design 146 (2019) 1104-1107
[6] DIEZ M. et al., In-situ observation of tungsten plasma facing components after the first phase of operation of the WEST tokamak, presented at IAEA 2021
[7] GALLO A. et al., First efforts in numerical modeling of tungsten migration in WEST with SolEdge2D-EIRENE and ERO2.0. Phys Scr. 1 janv 2020;T171:014013
[8] FIRDAOUSS M. et al., Fusion Engineering and Design 98-99 (2015) 1294-8
[9] GROSJEAN A. et al., 2020 Nucl. Fusion 60 106020
[10] DE TEMMERMAN G. et al., A growth/annealing equilibrium model for helium-induced nanostructure with application to ITER. Nuclear Materials and Energy. 1 mai 2019;19:255-61
[11] SAKAMOTO R. et al., Surface morphology of tungsten exposed to helium plasma at temperatures below fuzz formation threshold 1073 K. Nucl Fusion. 1 janv 2017;57(1):016040
[12] IALOVEGA M. et al., Hydrogen trapping in tungsten: impact of helium irradiation and thermal cycling. Physica Scripta. 1 janv 2020;T171:014066
[13] HIJAZI H. et al., Tungsten oxide thin film exposed to low energy He plasma: Evidence for a thermal enhancement of the erosion yield. Journal of Nuclear Materials. févr 2017;484:91-7
[14] BALDEN M. et al., Erosion and redeposition patterns on entire marker tiles after exposure in the first operation phase of WEST, presented at 18th Inter. Conf. on Plasma-Facing Materials and Components for Fusion applications, Unpublished to Phys. Scr. (in correction proofs round)
[15] MARTIN C. et al, 2013 J. Nucl. Mater. 438 S771-S774
[16] BREZINSEK S. et al., 2017 Nucl. Fusion 57 116041